

APPLICATION OF STATISTICAL TECHNIQUES TO THE ANALYSIS OF SOLAR CORONAL OSCILLATIONS

J. TERRADAS, R. OLIVER, AND J. L. BALLESTER

Departament de Física, Universitat de les Illes Balears, E-07122 Palma de Mallorca, Spain;
jaume@hubble.uib.es, ramon.oliver@uib.es, dfsjlb0@uib.es

Received 2004 March 25; accepted 2004 June 15

ABSTRACT

In this work, the application of two different techniques to the analysis of coronal time series is investigated. The first technique, called empirical mode decomposition, was developed by Huang and coworkers and can be used to decompose a signal in its characteristic timescales, allowing, among other applications, efficient filtration of the signal. The second technique, called complex empirical orthogonal function (CEOF) analysis, is an extension of the well-known principal component analysis, to which the Hilbert transform has been added. The CEOF analysis allows identification of the dominant spatial and temporal structures in a multivariate data set and is thus ideally suited to the study of propagating and standing features that can be associated with waves or oscillations. Here we apply both methods to time series obtained from a coronal loop and obtain detailed two-dimensional information about a propagating and a standing wave with periods around 5 and 10 minutes, respectively.

Subject headings: methods: statistical — Sun: corona — Sun: oscillations — waves

On-line material: color figures, mpeg animations

1. INTRODUCTION

In recent years the detection of oscillations in the solar atmosphere has provided a new tool for determining unknown coronal parameters. Measuring the properties of waves and oscillations, that is, finding out more information about the periods, wavelengths, amplitudes, temporal and spatial signatures, etc., together with the theoretical modeling of the wave phenomena, can be used as a seismic tool. In particular, coronal seismology has been widely developed in the context of the study of structures such as loops or prominences. In addition, the high spatial and temporal resolution of current satellite missions such as *TRACE* (Handy et al. 1999) or *SOHO* (Domingo et al. 1995) has allowed further development of the study of wave phenomena in the solar atmosphere. However, in order to obtain the maximum benefit from the data provided by satellites and ground-based instruments, it is necessary to apply suitable techniques to the analysis of coronal wave phenomena, and, in this respect, there are some key points that must be considered. The first issue is the noisy and nonstationary behavior of the time series, and the second issue is the two-dimensional (projected) character of propagating features.

Very often, signals of solar origin have a low signal-to-noise ratio, and sometimes to increase this ratio a new data set is created by summing over consecutive times, with a consequent reduction in the time resolution. Moreover, it is also common to integrate the signal over several neighboring points, which results in a decrease in spatial resolution. Finally, to emphasize the time variability of the analyzed data, a running-difference image is created by subtracting different frames with a threshold time step. Examples of the application of some of these methods to the analysis of solar coronal data can be found in Aschwanden et al. (2000) and De Moortel et al. (2000, 2002c). Although the final data can still retain some of the relevant features in the original signal, they are just averaged data with reduced temporal and spatial resolution. In order to try to avoid some of the previous shortcomings, an alternative approach consists in trying to separate the different timescales in the

signal. Hence, if noise can be efficiently isolated, it is possible to deal with the denoised signal without a temporal or spatial resolution sacrifice.

Another common feature of coronal time series is that they do not show stationary behavior. Oscillations are usually detected during a few periods and have a finite lifetime. As a consequence, Fourier spectral analysis (which requires the data series under study to be stationary) is of limited use. The Fourier spectrum of a signal requires many additional harmonic components to simulate nonstationary behavior, thus spreading the energy over a wide frequency range, and is unable to provide information about the lifetime of oscillations. Another limitation is that in this technique a linear superposition of trigonometric functions is used, so additional harmonics are needed to simulate deformed wave profiles associated with nonlinearity. On the other hand, wavelet analysis provides time localization of the frequency components, especially if the data show gradual frequency changes. Wavelet analysis has become popular and in recent years has been extensively applied to the analysis of different solar atmospheric oscillations (see Ofman et al. 2000; Banerjee et al. 2000; De Moortel et al. 2000, 2002a; O’Shea et al. 2001 for recent applications).

A very new and attractive method was recently developed by Huang et al. (1998, 1999). This statistical tool can be used to decompose a signal in its intrinsic timescales, which is particularly useful in dealing with nonstationary and even with nonlinear data and therefore satisfies the requirements for the analysis of solar time series. These authors show that the new method, whose key part is the empirical mode decomposition (EMD), can even overcome some of the limitations of the wavelet analysis, such as leakage and low time-frequency resolution. For these reasons, here we propose this method as a new tool for the analysis of coronal time series in order to isolate and study wave motions.

On the other hand, techniques designed to identify the dominant spatial and temporal structures in a data set are desirable, especially if one is interested in investigating

propagating and/or standing features that could be associated with waves. One of the simplest standard ways to detect a propagating disturbance in a field is to choose a particular path and then to plot, for different times, the values of the field along this path to obtain a time-distance image. The presence of one or more diagonal stripes in this image is a sign of coherent changes in position and time and consequently indicates propagation along the path, where the slope of the diagonal ridges in the image gives a measure of the propagation velocity of the feature. This method has been applied, for instance, to the analysis of propagating waves in loops (see Berghmans & Clette 1999; De Moortel et al. 2000, 2002b; Robbrecht et al. 2001), in plumes (see DeForest & Gurman 1998), and in prominences (see Terradas et al. 2002). However, the method provides only a partial picture of the motion, which is in general two-dimensional, allowing us to obtain information just along the particular selected path. An alternative approach to studying two-dimensional propagation is to compute the Fourier phase at each point in the data set and then to analyze its spatial distribution. Smooth changes of phase with position indicate the presence of a propagating wave, and the method produces satisfactory results if the wave shows a strong monoperiodic character (see Terradas et al. 2002). However, in most coronal signals there are several superposed oscillatory features that in some cases can be related to propagating and/or standing patterns, and hence, the application of the above-mentioned simple techniques can result in misleading conclusions. For these reasons, it is necessary to apply other adequate tools of analysis in order to obtain reliable information.

In this respect, there are statistical methods that have been developed and are routinely used in other areas of physics, such as climate and meteorological research, which include techniques of spatial and temporal pattern detection in multivariate data sets. These methods attempt to exploit the information available in spatially distributed data sets and involve eigenvalue decompositions. The most traditional technique is empirical orthogonal function (EOF) analysis, also known as principal component analysis. The goal of EOF analysis is to provide a compact description of the spatial and temporal variability of data series in terms of orthogonal functions or statistical “modes.” Usually, most of the variance of the spatially distributed time series is in the first few orthogonal functions, whose patterns may then be linked to possible dynamical mechanisms. EOF analysis only allows us to detect standing oscillations, but some extensions of this technique are very well suited to investigating propagating features, since they retain phase information in the decomposition. Complex empirical orthogonal function (CEOF) analysis in the time domain is an attractive and relatively simple alternative that allows for efficient detection of propagating features, especially when the variance is spread over a number of frequencies, and has provided satisfactory results in climate research (see Wallace & Dickinson 1972; Horel 1984).

The main purpose of this work is to describe and show the basic properties of the EMD method and CEOF analysis and to describe how they can provide valuable diagnostic information for coronal seismology. The EMD and CEOF techniques are explained in §§ 2 and 3, respectively. A real application of both tools to the analysis of loop oscillations is given in § 4, and finally, the main conclusions are drawn in § 5.

2. EMPIRICAL MODE DECOMPOSITION

EMD is based on the simple assumption that any data set is the sum of different simple intrinsic modes of oscillation. The

EMD method gives a decomposition of the signal into essentially band-limited components by using information from the signal itself instead of prescribing basis functions with fixed frequency, such as in Fourier analysis, or imposing a particular set of basis functions, as is the case with wavelet analysis. At the core of the EMD method is the idea that any data set is the sum of a few intrinsic mode functions (IMFs), since such a data set is the outcome of just a few physical processes intervening in the course of data generation and acquisition. (It must be emphasized, however, that there is no one-to-one correspondence between the physical processes and the IMFs obtained with the EMD method, since, for example, a nonlinear mechanism can give rise to the presence of different timescales in a signal, which would then be separated as different IMFs.) The next key idea is that each IMF has its very own timescale of variations, with oscillations that are symmetric about the local zero mean. These topics have been discussed at length in Huang et al. (1998, 1999), where further information, extensive discussions on the foundations of this technique, and many applications to synthetic and natural signals can be found (see also Komm et al. 2001).

2.1. Method

From their definition above, the intrinsic mode functions must fulfill the following restrictions:

1. For each IMF, the number of extrema and the number of zero crossings must either be equal or differ at most by 1.
2. For each IMF, the mean value of the envelope defined by the local maxima and the envelope defined by the local minima must be zero for all times.

The first condition is a global narrowband requirement, which ensures that periods that are too different are not mixed together in an IMF. The second restriction adds the local requirement that oscillations are about the zero level. Strange as these properties may seem, they are fulfilled by the well-known Fourier and wavelet basis functions: they are monoperiodic and have zero mean (and thus satisfy conditions 1 and 2, respectively.) With this definition, an IMF component is characterized by a single pair of amplitude and period values, which usually change in time. In this regard, the EMD method is a generalization of decomposing a stationary signal into trigonometric functions, which have constant amplitudes and frequencies.

For a given signal, $X(t)$, the EMD decomposition is performed in the following steps:

1. First, all local extrema are identified, and then the local maxima are connected by a cubic spline line, which gives the upper envelope.
2. This procedure is repeated for the local minima to obtain the lower envelope.
3. The mean of the upper and lower envelopes is designated $m_1(t)$, and the difference between the data and this mean is the first component, $h_1(t)$, that is,

$$h_1(t) = X(t) - m_1(t). \quad (1)$$

Ideally, $h_1(t)$ should be an IMF because the construction of $h_1(t)$ described above should have made it satisfy all the requirements of an IMF. However, overshoots/undershoots and “riding waves” are common in real signals and can generate new extrema. These and other effects are discussed at length by Huang et al. (1998), who indicate that the above procedure must be repeated several times until a true IMF is extracted. A

“sifting” process is then set up by which $h_1(t)$ is treated as the data and the above steps are repeated by taking

$$h_{11}(t) = h_1(t) - m_{11}(t). \quad (2)$$

After repeated sifting, say, up to k times, we finally end up with $h_{1k}(t) = h_{1(k-1)}(t) - m_{1k}(t)$, which is a true IMF. Then,

$$c_1(t) = h_{1k}(t) \quad (3)$$

is the first IMF component in the signal.

The sifting process must be applied with care, since the requirement that the local mean has to be zero can drive the process toward a pure frequency-modulated IMF with constant amplitude. To guarantee that the IMF components retain enough physical meaning with respect to both amplitude and frequency modulations, a stopping criterion for the sifting process must be introduced. Huang et al. (1998) suggest using a sort of standard deviation calculated from two consecutive siftings,

$$\sigma = \sum_{t=0}^T \left[\frac{|h_{1(k-1)}(t) - h_{1k}(t)|^2}{h_{1(k-1)}^2(t)} \right], \quad (4)$$

and stopping the iterative process when σ is smaller than a given value, σ_{\max} , that Huang et al. (1998) suggest can be set between 0.2 and 0.3. In our application of the method to the analysis of coronal data (§ 2.2) we have found that smaller values of this parameter (between 0.1 and 0.2) generally yield better results.

The first IMF, $c_1(t)$, contains the finest scale, or the shortest period component of the signal. We can separate $c_1(t)$ from the rest of the data by computing the residue, $r_1(t)$,

$$r_1(t) = X(t) - c_1(t). \quad (5)$$

Since this residue still contains longer period components, it is treated as new data and is subject to the same sifting process as described above. This procedure can be repeated to obtain all the subsequent $r_j(t)$ and $c_j(t)$, and the result is a series of residues and IMFs given by

$$r_2(t) = r_1(t) - c_2(t), \quad (6)$$

$$r_3(t) = r_2(t) - c_3(t), \quad (7)$$

...

$$r_n(t) = r_{n-1}(t) - c_n(t). \quad (8)$$

The process of extracting the IMF components can be finally stopped by any of the following predetermined criteria: either when the maximum of $|c_n(t)|$ or of $|r_n(t)|$ becomes so small that it is less than a predetermined value or when the residue $r_n(t)$ becomes a function from which no more IMFs can be extracted. This happens when the residue is either a constant or a function with long-term variations compared with the time span. This second condition translates into counting the number of extrema of the residue and stopping the iterations when that number is equal to 2 at most.

From equations (5)–(8), the original signal can now be reconstructed as

$$X(t) = \sum_{j=1}^n c_j(t) + r(t). \quad (9)$$

Thus, a decomposition of the data into n empirical modes is achieved, with a final residue, $r(t) \equiv r_n(t)$, which is simply the mean trend of the signal. Hence, the EMD method can effectively subtract the trend or mean value from the original series without any distortion in the information contained in the remaining data.

From the numerical point of view, the EMD decomposition is, in principle, quite clear and simple. However, the extension of the time series at the end points must be addressed. Upper and lower values for the envelopes at those particular points must be computed using the spline fitting. If these points are left unattended, cubic splines can diverge and show large swings. These swings can propagate inward and corrupt the data, especially if the data series is short. In order to avoid this problem, extra extrema must be added at each end of the signal, a possible solution being to extend the original data series by using a characteristic wave method. Huang et al. (1998, 1999) do not give many details as to how this extension must be implemented, so we have followed this approach: the maximum and minimum closest to the beginning or the end of the series are identified, and the characteristic wave period is defined as twice the time between them. Then, three more maxima and minima are added outside the time range of the signal with a time spacing given by the previously determined characteristic period. Note that since splines are fitted only to the extrema of the signal, this extension must be performed only with maxima and minima.

One of the biggest benefits of the EMD method is that it can be used as a novel filter. Traditionally, filtering is carried out in frequency space only, but there is a great difficulty in applying the frequency filtering when the data are either nonlinear, nonstationary, or both, and in general, harmonics are generated at all frequencies. By performing the EMD decomposition, the different coexisting modes of oscillation in the signal are separated, and so, for example, a low-pass filtering of the signal can be obtained by performing the sum of the last components and the trend in equation (9). Similarly, summing only the first IMF components results in a high-pass-filtered series, while performing the sum in equation (9) without the first and last components and the trend results in a bandpass-filtered time series. The advantage of this time-space filtering is that the results preserve the full nonlinearity and nonstationarity.

2.2. Application of EMD to Coronal Data

In order to show the advantages of the EMD method, we have analyzed some time series that are part of the data set studied in § 4. Since the data are described in more detail later, it suffices to mention here that the duration is 1240.8 s and that the time step between successive observations is 8.8 s, so there are a total of 141 values. The time series and its IMF components are shown in Figure 1; it can be appreciated that the signal is quite noisy but still some of the IMFs show oscillatory features with different timescales and amplitudes. The EMD method decomposes this signal in just six functions, namely, the six IMFs $c_1(t)$ to $c_5(t)$ plus the trend $r(t)$, instead of the tens of modes (141 in this particular example) that would be required had a Fourier expansion been used to represent the whole data set. Moreover, this technique separates the data into locally nonoverlapping timescale components that display oscillations about the zero level. The first component, c_1 , contains only small timescales with large amplitudes, which are characteristic of noise in this particular signal. Components c_2 – c_4 have larger periods, roughly in the range 1–4 minutes. However, the most noticeable IMF component is c_5 , which is

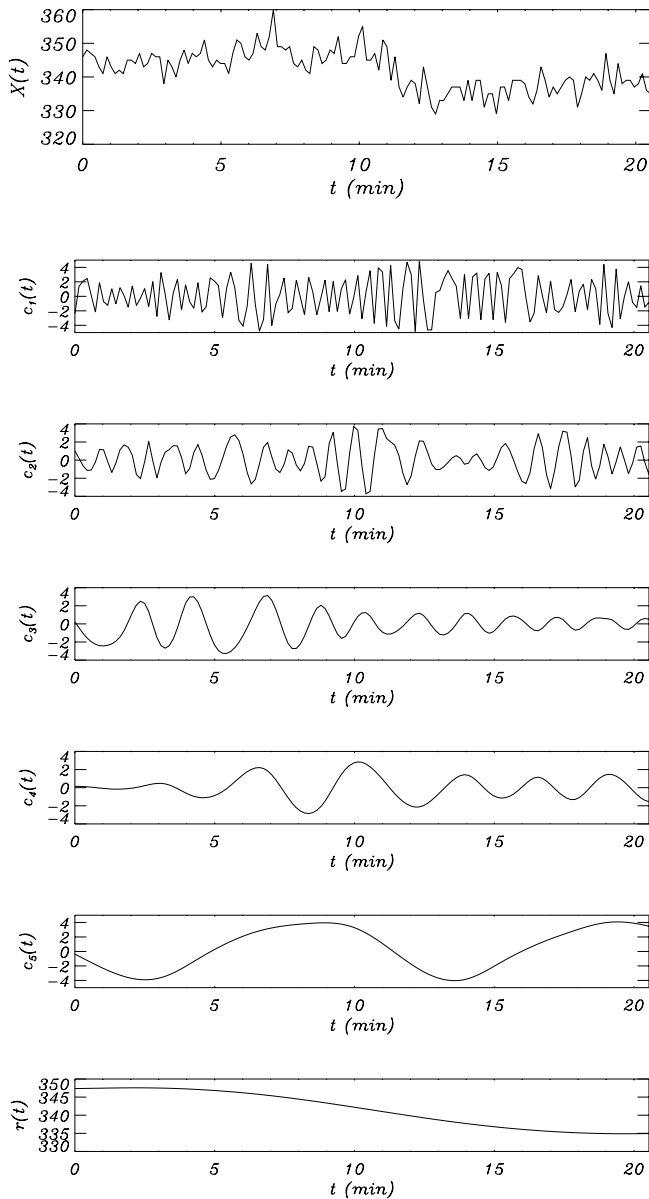


FIG. 1.—Top panel displays the signal analyzed with the EMD method, while the next five panels show the resulting IMF components, $c_1(t)$ – $c_5(t)$. Each component has its own characteristic amplitude and its own timescale, which is small for $c_1(t)$ and becomes increasingly larger for the subsequent IMFs. The bottom panel shows $r(t)$, which is not truly an IMF but is merely the trend. In the decomposition of the signal, an IMF is accepted during the sifting process when σ defined in eq. (4) becomes smaller than $\sigma_{\max} = 0.2$.

quite symmetric and has a period around 10 minutes. Note that, although this component has a small amplitude in comparison with the first, noisy component, it is nevertheless decomposed as an IMF.

Once the IMF components have been computed, we can easily reconstruct the original signal. In Figure 2a we have plotted the original data and the long-term residual trend. When the last component, c_5 , is added to the trend, the fitting to the original data is improved and part of the oscillatory character of the signal is recovered (see Fig. 2b). By successively adding more IMF components with smaller periods, the results shown in Figures 2c–2f are obtained. Note that by adding components up to c_3 we have recovered practically all the original signal, while the rest of the components essentially add short-term variability but little more information. From these

results it is clear that the EMD method is a useful tool for analyzing a signal and isolating the different timescales, which may be associated with different physical processes. Therefore, those components that seem to have a particular physical meaning can be extracted from the signal and a detailed analysis of each of them can be performed separately.

Finally, the EMD is a useful filtering tool, since one can confidently “clean” the noise in the signal by removing its first IMFs and also subtract the trend by removing the residue. It is quite striking that, for our loop data, by changing σ_{\max} between 0.05 and 0.3, both $c_1(t)$ and $r(t)$ remain practically unchanged, while the details in the other components may differ between the various decompositions. Therefore, the EMD method is quite robust in getting the right noise and trend despite using different values of σ_{\max} in the stopping criterion. This is the reason why the EMD is used in the task of noise and trend removal in the preparation of the data set in § 4.

3. COMPLEX EMPIRICAL ORTHOGONAL FUNCTION ANALYSIS

The complex EOF analysis is a multivariate technique devised to obtain the dominant spatial patterns of variability in a statistical field. As the CEOF approach has considerable potential for being widely used to analyze propagating phenomena and is not a common technique in the analysis of solar data, we give in the following a brief overview of the method. For further details the reader is referred to Wallace & Dickinson (1972), Horel (1984), and von Storch & Zwiers (1999). It should be mentioned that the last authors refer to this tool as Hilbert EOF analysis.

3.1. Method

The purpose of classical EOF analysis is to identify patterns that characterize variations in the current “state” of a scalar field, which means that the technique does not efficiently take into account the time evolution of the analyzed field. A means of accounting for such time evolution is to quantify the time series in terms of complex numbers by adding to it its Hilbert transform, which gives information about the rate of change of the field, as an artificial imaginary part. The result is that the information contained in the Hilbert scalar field is greater than that in the original field.

Let $X(\mathbf{x}, t)$ be a scalar field representing a time series, where \mathbf{x} corresponds to spatial position and t to time. At a particular location \mathbf{x}_j this field can be written as

$$X(\mathbf{x}_j, t) = \sum_{\omega} a_j(\omega) \cos(\omega t) + b_j(\omega) \sin(\omega t), \quad (10)$$

where $a_j(\omega)$ and $b_j(\omega)$ are the Fourier coefficients and the sum is carried over all Fourier frequencies. In order to describe the propagating features in the scalar field the original data set is written in terms of the complex representation

$$U(\mathbf{x}_j, t) = \sum_{\omega} c_j(\omega) \exp(-i\omega t), \quad (11)$$

where $c_j(\omega) = a_j(\omega) + ib_j(\omega)$. An expansion of the exponential term in equation (11) yields

$$\begin{aligned} U(\mathbf{x}_j, t) &= \sum_{\omega} \{ [a_j(\omega) \cos(\omega t) + b_j(\omega) \sin(\omega t)] \\ &\quad + i [b_j(\omega) \cos(\omega t) - a_j(\omega) \sin(\omega t)] \} \\ &= X(\mathbf{x}_j, t) + i\hat{X}(\mathbf{x}_j, t), \end{aligned} \quad (12)$$

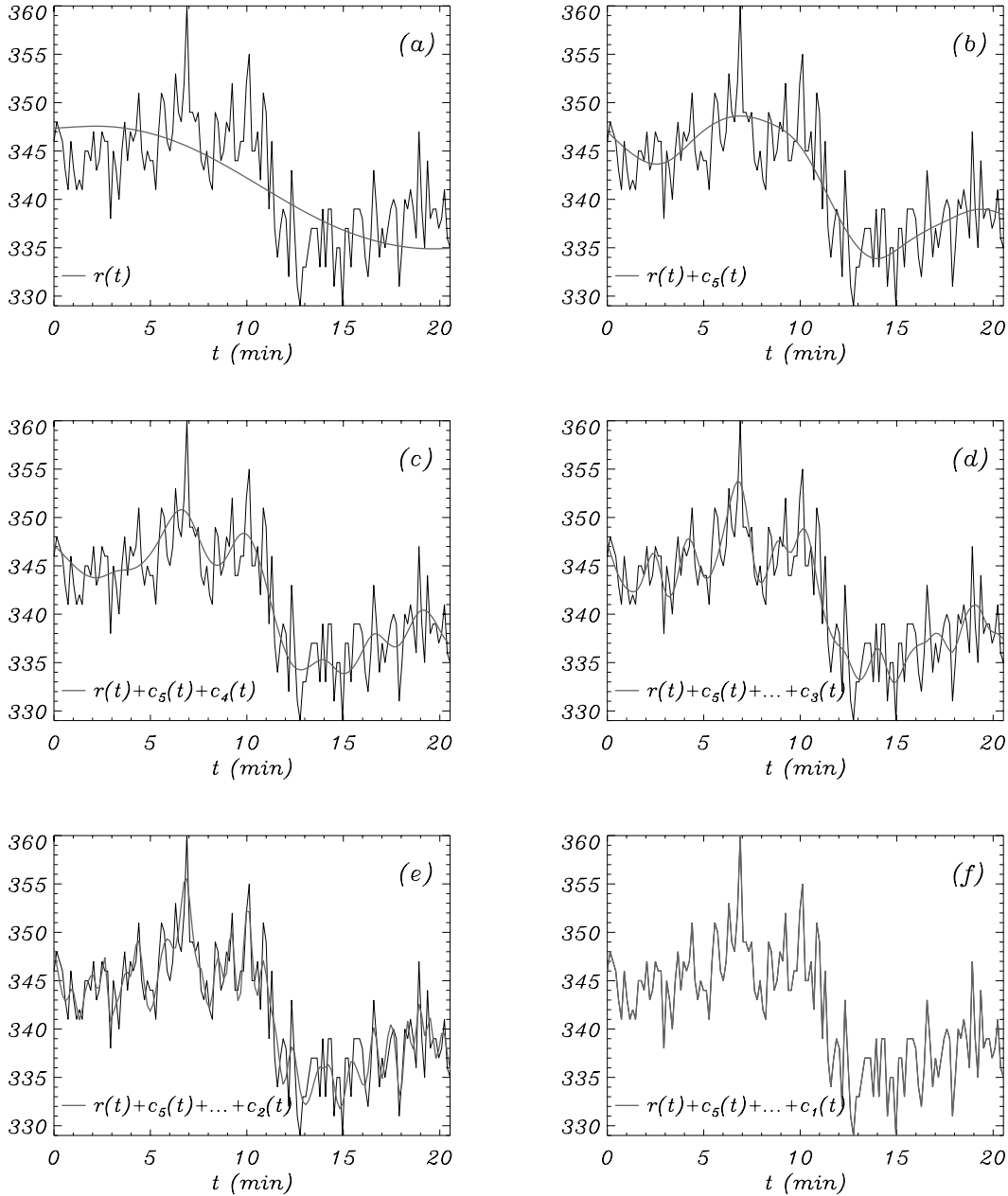


FIG. 2.—Reconstruction of the original data from the IMF components shown in Fig. 1. (a) Data (*thin line*) and the trend (*thick line*). (b) Data and the sum of the trend and the last component, c_5 . (c–f) Same as (b) with an additional IMF component added in each plot.

where the real part is simply the original data array and the imaginary part is its Hilbert transform and represents a filtering operation upon $X(x_j, t)$ in which the amplitude of each Fourier spectral component is unchanged while its phase is advanced by $\pi/2$.

Next, the covariance matrix, C , is defined by means of

$$C_{ij} = \langle U^*(\mathbf{x}_i, t)U(\mathbf{x}_j, t) \rangle_t, \quad (13)$$

where the asterisk denotes complex conjugation and $\langle \dots \rangle_t$ indicates time averaging. Here C represents the cross-spectral matrix and by construction is Hermitian and possesses m real, nonnegative eigenvalues, λ_n , and complex eigenvectors, $E_n(\mathbf{x})$, $n = 1, 2, \dots, m$. Once the spatial eigenvectors are calculated, their corresponding time evolution is given by the time series $A_n(t)$, which is obtained by projecting the complex data series

$U(\mathbf{x}, t)$ onto the proper eigenvector $E_n(\mathbf{x})$ and summing over all locations

$$A_n(t) = \sum_j U(\mathbf{x}_j, t)E_n(\mathbf{x}_j). \quad (14)$$

By definition, the n th CEOF mode consists of a spatial part, i.e., the pattern $E_n(\mathbf{x})$, and a temporal part, the principal component $A_n(t)$, such that the product $E_n^*(\mathbf{x})A_n(t)$ corresponds to a representative oscillatory component present in the field. As a consequence, the spatial and temporal behavior of the n th mode can then be derived by taking the real part of $E_n^*(\mathbf{x})A_n(t)$. The original complex data field, $U(\mathbf{x}, t)$, can be totally reconstructed by adding this product over all modes,

$$U(\mathbf{x}, t) = \sum_{n=1}^m E_n^*(\mathbf{x})A_n(t). \quad (15)$$

Therefore, the field has been decomposed in a sum of empirically derived basis functions that represent different features present in the data. And even more important, there is a simple way of quantifying the contribution of each mode to the total field, since the n th complex EOF is associated with a fraction of the total field variance given by

$$\frac{\lambda_n}{\sum_{l=1}^m \lambda_l}. \quad (16)$$

With the above decomposition, if there are several coherent oscillatory structures propagating in a field, each wave pattern will be separated into its own eigenmodes by the CEOF analysis. The most dominant pattern in the data set will have the largest eigenvalue, i.e., the largest fraction of the total variance, and since the eigenvalues are sorted for convenience in descending order, the largest eigenvalue corresponds to the first one.

Since the terms in equation (15) are complex numbers, the field U can be expressed as

$$U(\mathbf{x}, t) = \sum_{n=1}^m S_n(\mathbf{x}) e^{-i\theta_n(\mathbf{x})} R_n(t) e^{i\phi_n(t)}, \quad (17)$$

and four measures that define possible moving features in $X(\mathbf{x}, t)$ can be defined immediately without any assumption about the field:

1. *Spatial amplitude function.*—This measure shows the spatial distribution of variability associated with each eigenmode and may be interpreted as in normal EOF analysis. The definition of the spatial amplitude function associated with the n th eigenmode is

$$S_n(\mathbf{x}) = [E_n(\mathbf{x})E_n^*(\mathbf{x})]^{1/2}. \quad (18)$$

The spatial distribution of S_n gives a measure of spatial homogeneity, by mode, in the magnitude of the X field.

2. *Spatial phase function.*—This function shows the relative phase fluctuation among various spatial locations where X is defined. This measure varies continuously between $-\pi$ and π , and as such, it is no longer restricted to the two possible values it can take in standard EOF analysis (namely, 0 or π). The spatial phase associated with the n th eigenmode is defined as

$$\theta_n(\mathbf{x}) = \arctan \left[\frac{\text{Im}(E_n(\mathbf{x}))}{\text{Re}(E_n(\mathbf{x}))} \right]. \quad (19)$$

3. *Temporal amplitude function.*—A measure of temporal variability in the magnitude associated with the n th eigenmode in the X field is obtained from

$$R_n(t) = [A_n(t)A_n^*(t)]^{1/2} \quad (20)$$

and may be interpreted as the principal component in standard EOF analysis.

4. *Temporal phase function.*—Finally, the temporal phase describes the temporal variation of the phase of the n th eigenmode associated with periodicities in the field X and is defined as

$$\phi_n(t) = \arctan \left[\frac{\text{Im}(A_n(t))}{\text{Re}(A_n(t))} \right]. \quad (21)$$

One of the limitations of the CEOF analysis is related to the end effects in the time series when the Hilbert transform is computed, which can be especially significant for long-period modes. Another feature of the method related to the Hilbert transform is the tendency to emphasize modes that oscillate at the Fourier frequencies. On the other hand, the CEOF analysis is particularly useful when the signal shows a stationary or weakly nonstationary behavior. Otherwise, this technique can introduce extra modes, with similar variances, to explain nonstationarity (see § 4), but even in this case it is still possible to extract useful information from the analyzed field.

3.2. Example

In order to show the basic properties of the CEOF analysis and to help interpret the above-mentioned four measures, we apply this technique to the following synthetic two-dimensional field (the data set consists of a time series of 300 samples over a grid of 21×21 points):

$$X(x, y, t) = \left[4 \sin 2\pi \left(\frac{x}{15} \right) \sin 2\pi \left(\frac{t}{100} \right) + 2 \sin 2\pi \left(\frac{x}{6} - \frac{t}{30} \right) \right] \times e^{-[(y-10)/4]^2} + N(t). \quad (22)$$

This simple example represents the superposition of a standing wave and a propagating wave in the x -direction. Both waves have different amplitudes, periods, and wavelengths and are confined in the y -direction around $y = 10$ by a Gaussian profile. The standing and the propagating waves have amplitudes, in arbitrary units, of 4 and 2, periods of 100 and 30, and wavelengths of 15 and 6, respectively. In addition, white noise uniformly distributed between -1.5 and 1.5 , $N(t)$, has been added to the field.

The application of the CEOF method to the field X allows the signal to be decomposed in several modes with different variances. From equation (16), the first two modes account for 25% and 12% of the total variance, respectively. The variance of the first mode doubles that of the second mode, since the ratio of their amplitudes is 4 : 2. The rest of the modes, which are associated with the simulated noise, contribute smaller variance (less than 1% each) to recover 100% of the total variance of the field. In Figure 3 we have plotted the temporal and spatial amplitude and phase functions, i.e., $R(t)$, $\phi(t)$, $S(x, y)$, and $\theta(x, y)$, for the first two modes. For both modes we can see that the temporal amplitude does not change considerably in time; i.e., $R(t)$ is approximately constant and shows small-scale variations introduced by the noise, which can in principle be eliminated if the initial field is filtered (for example with the EMD method). We can also see that the temporal phase varies linearly in time; i.e., $|\phi(t)| = \omega t$. Hence, the time derivative of $\phi(t)$ is a measure of the “instantaneous” frequency, which is different for these two modes. Estimations of the period, computed from a linear least-squares fit to the phase, give values of 100 and 30 for the first and second modes, respectively, as expected. Note that from the definition of temporal (and spatial) phase, these measures take values between $-\pi$ and π and therefore the phases must usually be corrected, i.e., unwrapped, in order to have smooth spatial or temporal variations, free of inconvenient jumps of 2π rad. We have applied specific algorithms to correct the phases, but in some cases this problem is difficult to solve, especially for noisy signals.

Regarding the spatial amplitude, $S(x, y)$, of the first mode, we can see that it is different from zero in a region localized

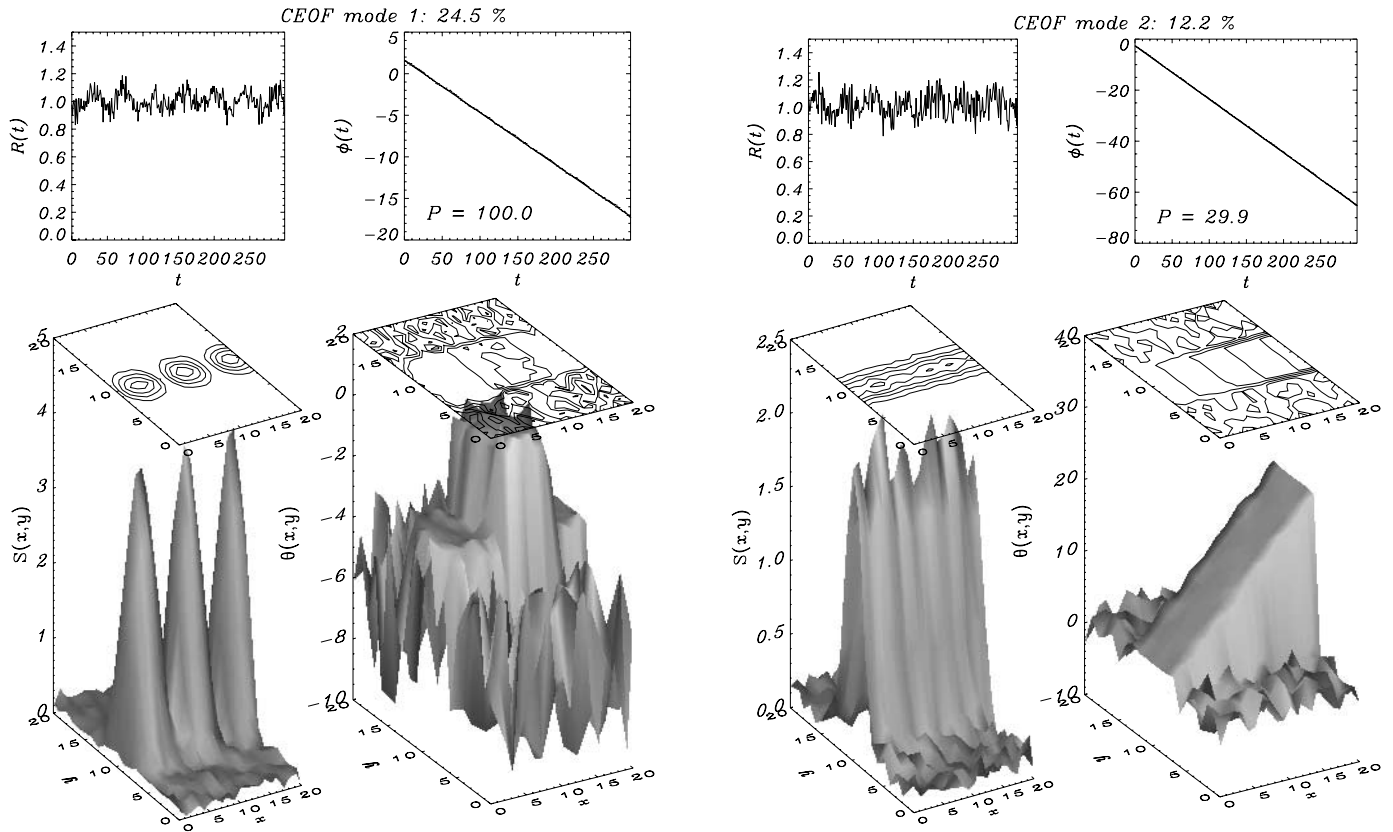


FIG. 3a

FIG. 3b

FIG. 3.—Four magnitudes defined by eqs. (18)–(21), which correspond to (a) the first mode (25% of the field variance) and (b) the second mode (12% of the field variance) in the CEOF decomposition of the field given by eq. (22). The two modes represent the standing and traveling part of the signal, respectively. The temporal amplitude is practically constant for both modes, although it shows fluctuations introduced by noise. The slope of the temporal phase, $\phi(t)$, gives the value of the frequency for each mode. The spatial information, contained in $S(x, y)$ and $\theta(x, y)$, has a rather different behavior for the two modes. For the first one, the amplitude shows the location of nodes and antinodes, while the phase has a jump of π between the antinodes as corresponds to a standing wave. For the second mode, which represents a traveling wave, the spatial amplitude is simply the Gaussian function in the y -direction and the spatial phase increases linearly in the x -direction, its gradient being the wavevector. [See the electronic edition of the Journal for a color version of this figure.]

around position $y = 10$, where the structure of nodes and antinodes that corresponds to a standing wave becomes evident. The wavelength can be calculated in this case as the distance between the first and third maxima of the amplitude, which gives a value of 15. As the first mode corresponds to the standing wave, its spatial phase $\theta(x)$ shows a jump of π rad between the antinodes in the region $7 \lesssim y \lesssim 13$, while it takes random values elsewhere. On the other hand, the second mode, which corresponds to the propagating feature, shows rather different behavior. The spatial amplitude is roughly constant in x and delineates the Gaussian profile in the y -direction, while the spatial phase varies linearly with distance, i.e., $\theta(x) = kx$, for $7 \lesssim y \lesssim 13$. Thus, the spatial derivative of $\theta(x)$ provides a measure of the “local” wavenumber, the variation of the spatial phase with position being a consequence of the traveling character of the wave. The estimation of the wavelength gives a value of 6. Therefore, the main features of the signal have been efficiently determined in spite of the large amount of noise present in the data. In addition, the sum of the first two modes in the form given by equation (15) allows one to reconstruct the meaningful spatial patterns in our synthetic signal.

4. APPLICATION TO LOOP OSCILLATIONS

The EMD method is applied to *TRACE* 171 Å (Fe IX) intensity observations of active region AR 8496 on 1999 March 23,

in which De Moortel et al. (2000) found short-period propagating waves originating at a footpoint of a large loop. The sequence consists of 141 512×512 pixel images with 8.8 s cadence and total duration of 20.68 minutes. The pixel size is $1''$, and the intensity values are given in DN (digital number). We have restricted the analysis to the large loop structure located far from the active region (see Fig. 4a and the top panel of the associated mpeg, Movie 1, available in the online *Journal*). No flare occurred near the time of the observations, and the loop did not show significant changes in its structure, although the image underwent a slight drift toward the right because of solar rotation. However, because of the short duration of the time series, the rotation effect is very small and has not been corrected. The data reduction was carried out using the standard *TRACE* IDL SolarSoftWare utilities (see Freeland & Handy 1998).

We first performed the EMD analysis of the temporal series at each spatial point in Figure 4a. As a consequence, we have a collection of several IMF components and the residual trend at each spatial location. In order to analyze the results of the decomposition, we have built a movie of the temporal evolution of the whole region with just the contribution of the computed trend (see Movie 1, *bottom panel*). The movie shows a smooth temporal evolution of the structure in which low-period components have been efficiently eliminated,

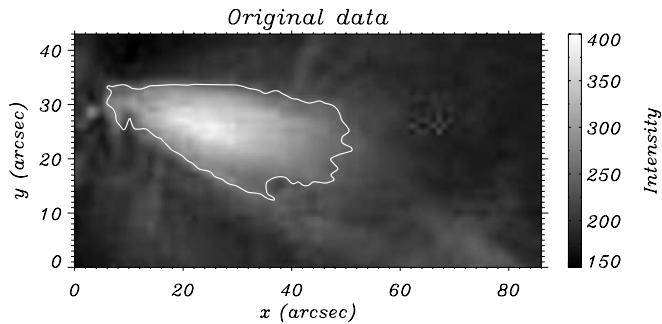


FIG. 4a

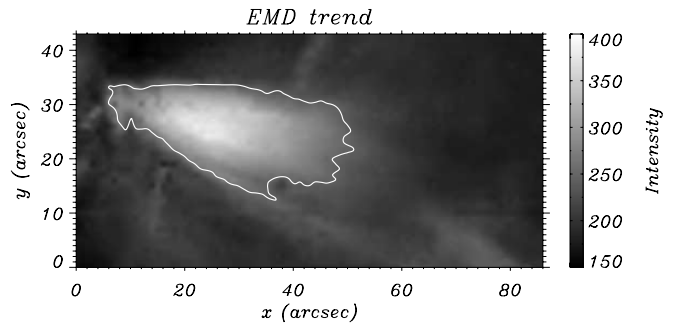


FIG. 4b

FIG. 4.—(a) Image of the 171 Å data set at the beginning of the observing time (06:55:02 UT 1999 March 23). The image in (b) was obtained by first applying the EMD to the intensity time series of each of the 86×43 spatial points. The obtained trends have been put together to make a movie (*bottom panel in Movie 1*) whose first frame is shown in (b). In both images the white line delineates the edge of the loop, determined as the contour level with intensity 250 DN at 07:12:38 UT. [See the electronic edition of the *Journal* for a color version of this figure.] This figure is also available as an mpeg animation in the electronic edition of the *Astrophysical Journal*.

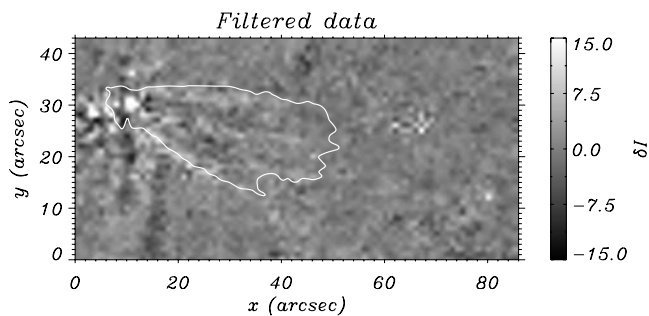


FIG. 5a

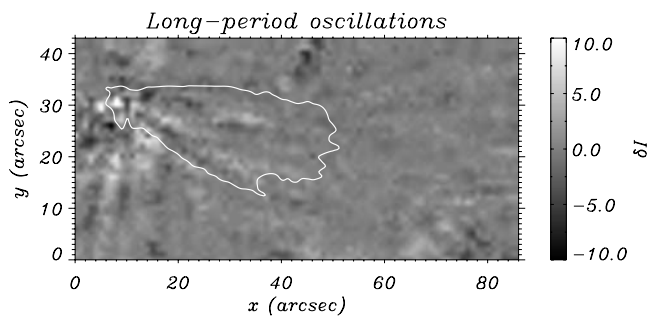


FIG. 5b

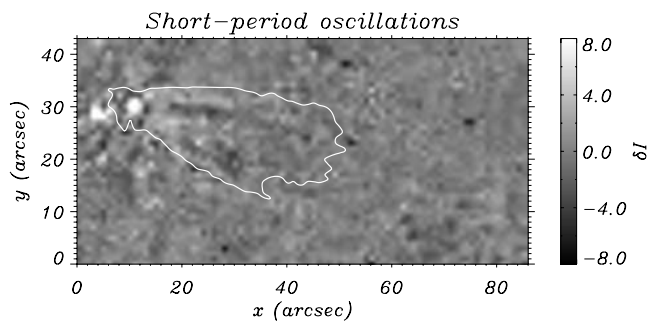


FIG. 5c

FIG. 5.—Three panels corresponding to the first frame in *Movie 2*. (a) Original time series (i.e., top panel in *Movie 1*) with the EMD trend and noise subtracted. (b) Temporal evolution of the first CEOF mode, with period 10.7 minutes. (c) Temporal evolution of the third and fourth CEOF modes, whose periods are 5.3 and 4.3 minutes. The white line delineates the edge of the loop at 07:12:38 UT. [See the electronic edition of the *Journal* for a color version of this figure.] This figure is also available as an mpeg animation in the electronic edition of the *Astrophysical Journal*.

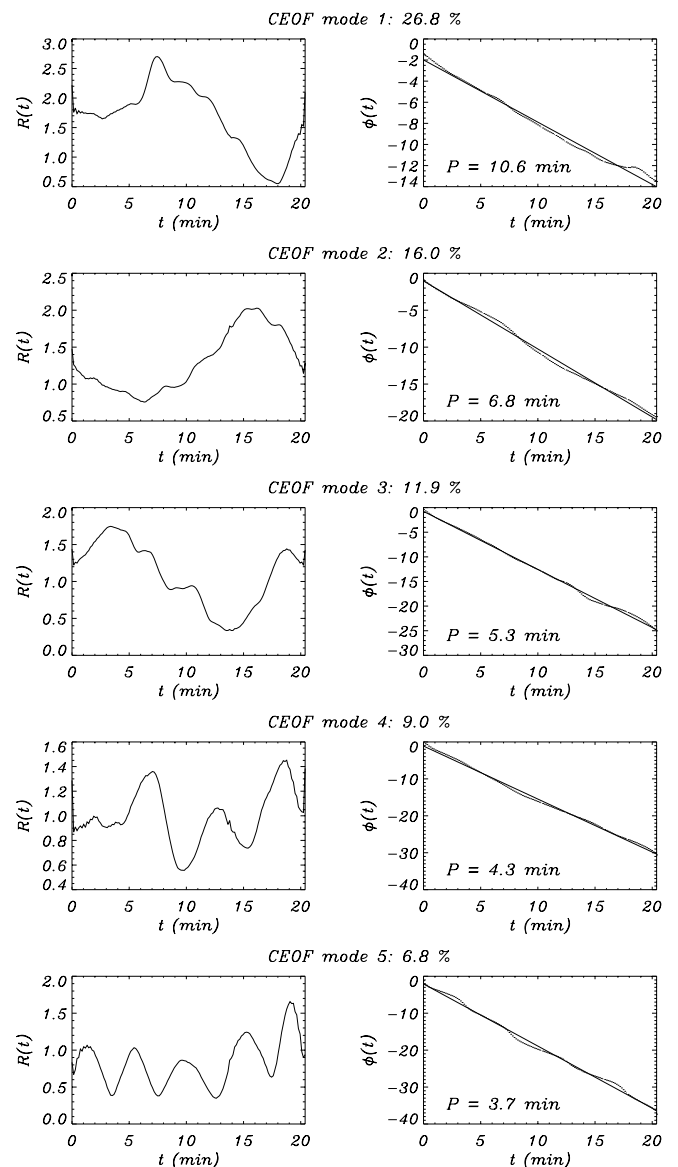


FIG. 6.—Analysis of the data in the top panel of *Movie 2*: temporal modulus and phase of the first five CEOF modes. The period of each mode, computed from a linear least-squares fit to the phase (*solid line*), and the percentage of the total field variance accounted for by the mode are given.

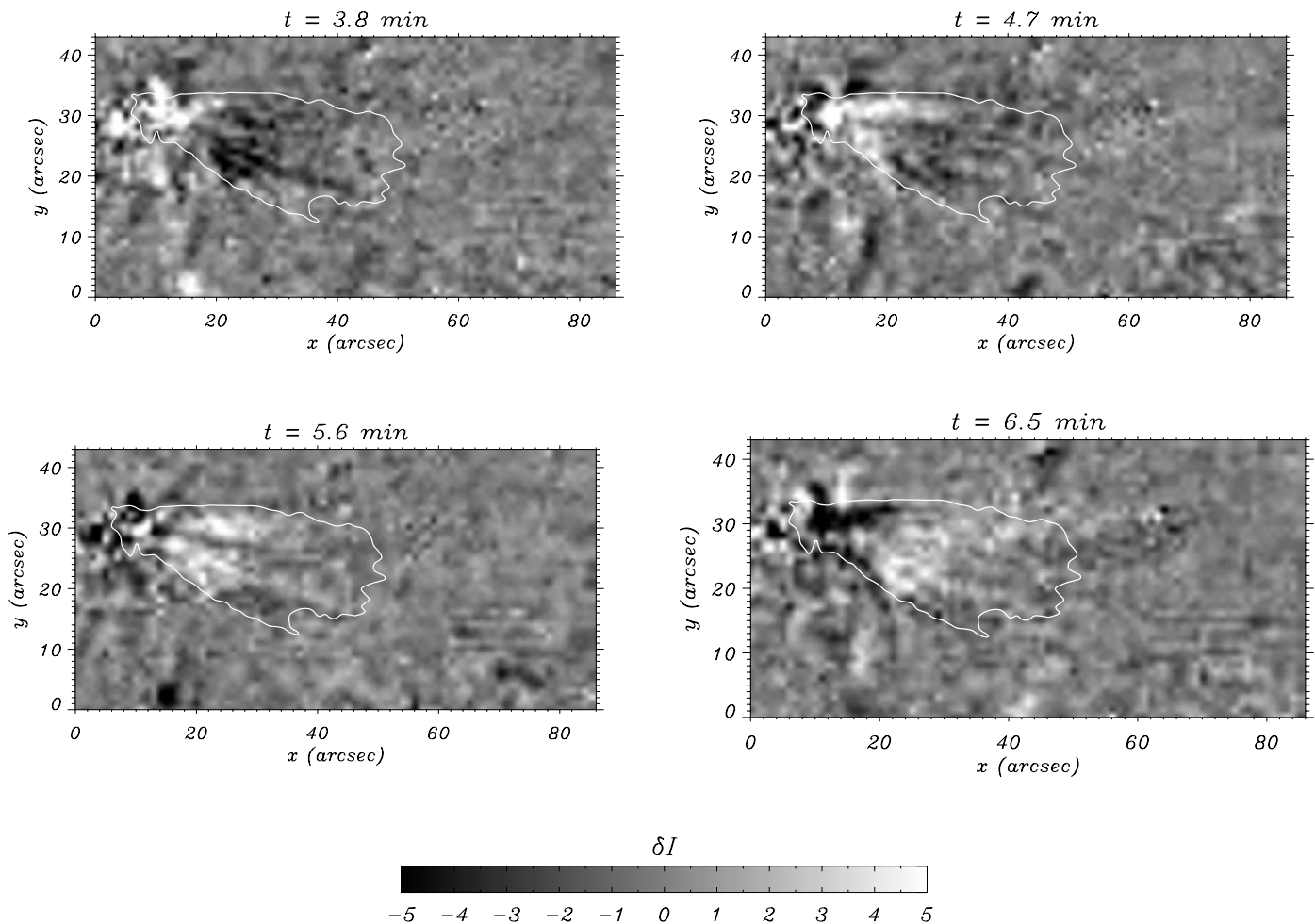


FIG. 7.—Four frames of the movie of the CEOF modes displaying oscillations around 5 minutes (bottom panel in Movie 2). The time between consecutive frames is 52.8 s \sim 0.9 minutes. These plots clearly show the propagation of intensity fluctuations along the loop. For example, the white feature close to the footpoint (around position $x = 10$ and $y = 30$) in the first frame moves along the structure and 2.7 minutes later is located around $x = 30$ and $y = 25$, as can be seen in the last frame. The white line delineates the edge of the loop at 07:12:38 UT. [See the electronic edition of the *Journal* for a color version of this figure.]

resulting in a highly denoised image compared with the original data. Next, a movie of the contribution of the rest of the IMF components with periods greater than 2 minutes (below this period noise is highly dominant) has also been constructed. To this end, the fast Fourier transform of all the IMFs at each point were computed, and those components whose largest power peak lies below 2 minutes were discarded. The rest of the IMFs were added up to get a “filtered” time series with no noise and no long-term variations (see Fig. 5a and the top panel in Movie 2, its associated mpeg, available in the online *Journal*). This movie shows several interesting features, the most relevant ones being a strong periodicity, with large amplitudes, at the footpoint of the loop together with some wave propagation along the loop from its footpoint and the presence of some coherent features in the structure. Note the small amplitude of these variations in comparison with the loop intensity (compare Figs. 4 and 5). The small amount of spikes present in the data set do not make a significant contribution to the noise of the signal. The most important contribution to the noise is produced by the instrument, which according to the Poisson statistics is around $(0.08I + 2.8)^{1/2}$, with I the observed intensity expressed in DN (see Aschwanden et al. 2000; Robbrecht et al. 2001). For typical intensity values in the loop center (~ 340 DN) this formula gives an error in the intensity of

± 5 DN. Although some of the components of the EMD can have intensity fluctuations similar to this value, it is possible to discard, on the basis of their timescales, those that are directly related to noise from those that can have a physical meaning. For example, from Figure 1 we see that the first IMF component of the decomposition (c_1) is certainly related to noise because of its short-timescale variations and its amplitude of about 4 DN; nevertheless, the component c_4 has similar amplitude but a much longer characteristic time of oscillation, which suggests that this component represents some real mechanism. In fact, as we show later this component is related to the propagating feature in the data set.

In order to investigate these phenomena we have performed a CEOF analysis of the “filtered” data set, which reveals the presence of oscillations with rather different properties. The temporal modulus and phase of the first five CEOF modes are shown in Figure 6; in all cases, the temporal modulus varies strongly in time, and although the phase is rather constant in time, this points out the presence of nonstationary variations in the data. On the other hand, these five modes account for almost 71% of the total variance contained in the filtered signal, so we discard all other modes and concentrate on these. We next performed a reconstruction of the spatial and temporal structure of each CEOF mode by computing the product

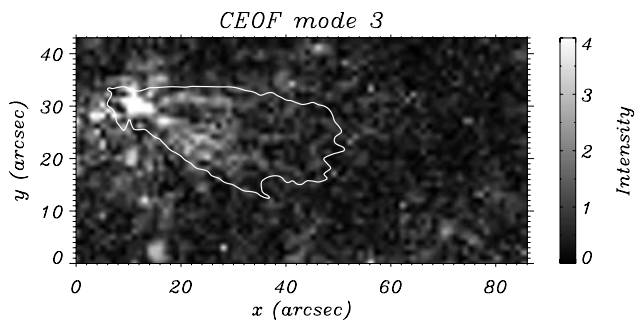


FIG. 8a

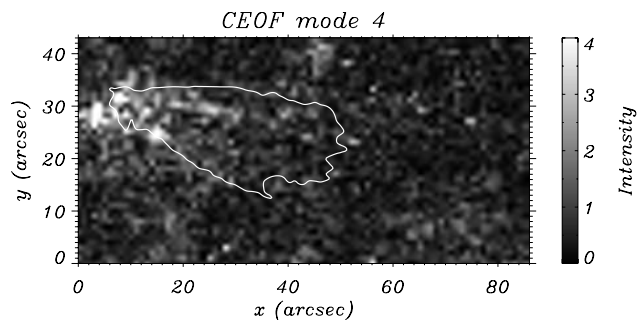


FIG. 8b

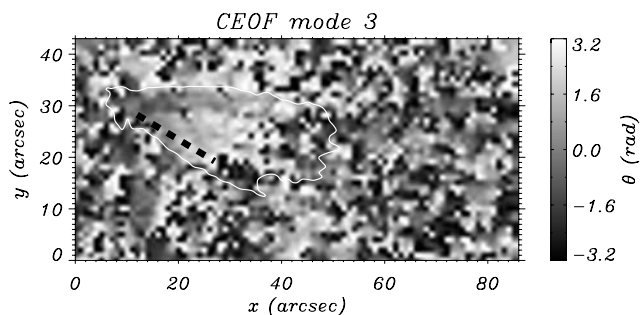


FIG. 8c

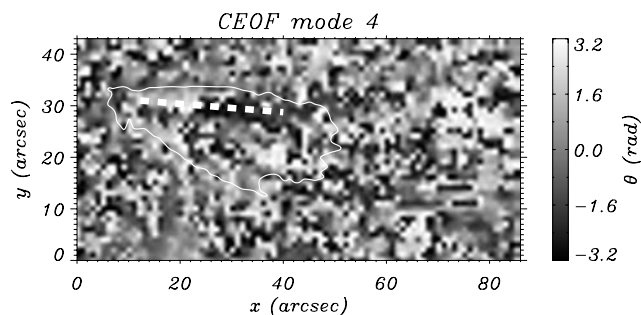


FIG. 8d

FIG. 8.—Distribution of the spatial amplitude, $S(x, y)$, for (a) the third mode and (b) the fourth mode in the CEOF analysis. In both cases the maximum amplitude is found at the footpoint of the loop; furthermore, for the first mode the amplitudes are roughly uniformly distributed across the loop structure. (c, d) Corresponding distribution of the spatial phase, $\theta(x, y)$. The dashed lines in (c) and (d) mark the selected paths for which the phase is represented in Fig. 9. [See the electronic edition of the *Journal* for a color version of this figure.]

$E_n^*(\mathbf{x})A_n(t)$; this shows the presence of two outstanding oscillatory features that are described next.

4.1. Oscillations with Period ~ 5 minutes

Here we start with a visual inspection of the temporal evolution of the CEOF modes with periods of 5.3 and 4.3 minutes, which account for 20.9% of the total variance of the “filtered” signal. It turns out that they both correspond to the propagating perturbation originating at the footpoint of the loop that can be appreciated in the “filtered” signal (Movie 2, *top panel*). For this reason, the two modes are part of the same physical phenomenon, but just because this phenomenon is probably nonstationary, the CEOF technique splits it into more than one mode. It is thus clear that these two CEOF modes must be considered together.

Thus, we next construct a movie with the temporal variation of the two modes together. The results can be seen in the bottom panel of Movie 2 (see also Fig. 5c) and in Figure 7, in which some frames of the movie for different times are displayed. These frames show that large intensity variations are located mainly in the loop and around its footpoint, while intensity variations outside the structure are much fainter. Organized intensity changes seem to be generated at the footpoint of the loop, then propagate along its length, and finally disappear around position $x = 40$. Note also the alternation between positive and negative intensity values, which is clear evidence of the existence of a propagating wave instead of a flow pattern along the loop. These oscillations are distributed over practically the entire projected width of the loop.

The periodic intensity changes are especially noticeable during the first half of the observational time. During the

second half, coherent oscillatory structures are more difficult to identify, which reflects the nonstationary character of the signal. Further support for this conclusion comes from the temporal information contained in the two CEOF modes (shown in Fig. 6): the first one displays a temporal amplitude with a global decrease in time, whereas the amplitude of the second mode oscillates in time. Since the range of variation of $R(t)$ is similar for both modes, the above implies that at a given time one of the two modes may dominate over the other. This must be interpreted as a consequence of the weak nonstationary character of the wave propagation pattern. It is to be noted that, owing to the small amplitude of intensity perturbations with respect to the background loop intensity, nonlinearity cannot be claimed here as the cause of this behavior.

On the other hand, the spatial amplitude and phase of the two CEOF modes also provide useful information. As we can see in Figures 8a and 8b, the spatial distribution of amplitudes is similar for the two CEOF modes and shares some interesting properties: large amplitudes are found close to the footpoint in both modes, whereas outside the loop and inside it but far from the footpoint the amplitudes are negligible. Moreover, the spatial modulus displays a clear decrease along the loop and is roughly uniformly distributed across the loop for the two modes, although the second one shows some signs of structuring. Thus, this pair of modes effectively captures the spatial distribution of the propagating disturbance inside the loop.

The spatial phase of the two modes is shown in Figures 8c and 8d; outside the loop the phase displays the expected random, small-scale variations that had already been found in the analysis of the synthetic signal (§ 3.2). On the other hand, inside the loop the phase shows some gradual variations,

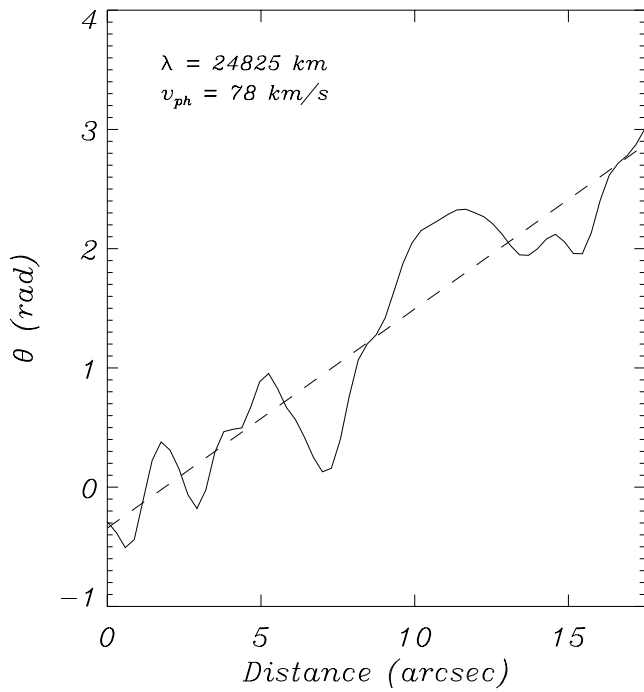


FIG. 9a

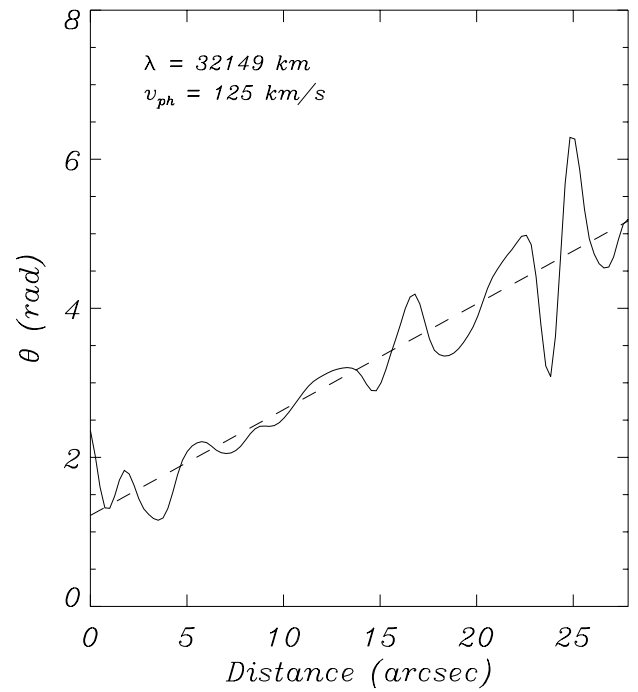


FIG. 9b

FIG. 9.—Phase variation vs. position along two particular paths inside the loop (see Figs. 8c and 8d). The dashed line is a linear fit that allows us to compute the value of the wavelength of the propagating wave. The phase speed has been estimated from the wavelength and the period.

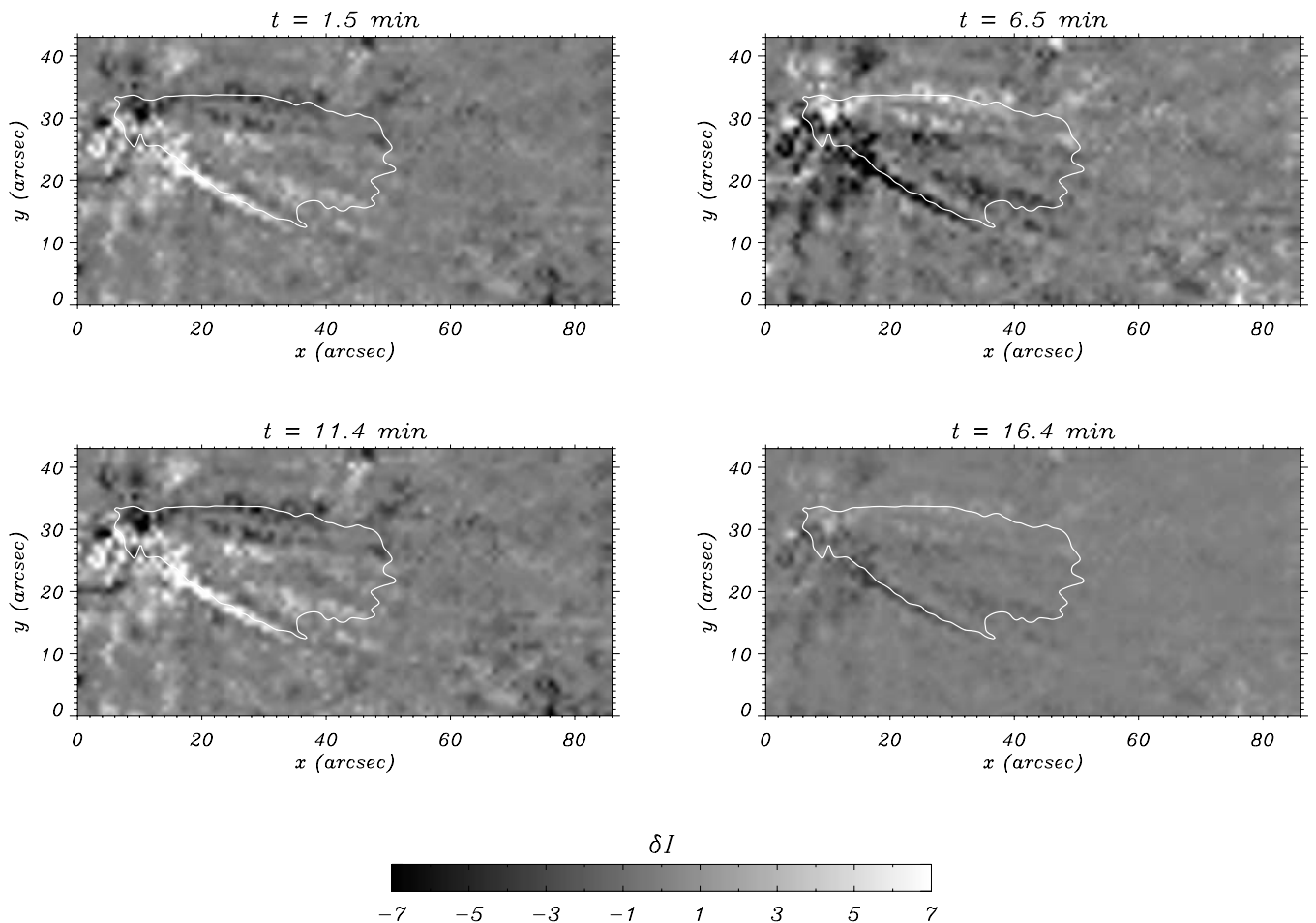


FIG. 10.—Four frames of the movie of the CEOF mode displaying oscillations around 10 minutes (middle panel in Movie 2). The time between consecutive frames is ~ 5 minutes. Oscillations are mainly located in thin filamentary structures inside and at the edges of the loop. The white line delineates the edge of the loop at 07:12:38 UT. [See the electronic edition of the Journal for a color version of this figure.]

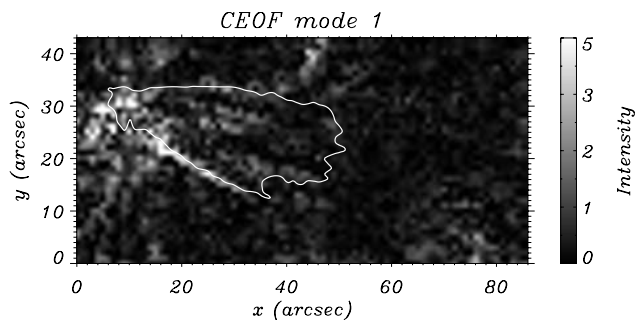


FIG. 11a

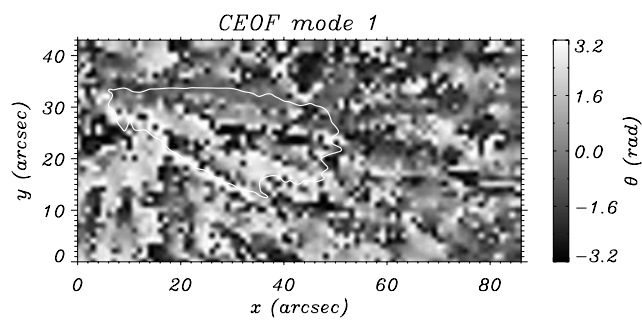


FIG. 11b

FIG. 11.—(a) Distribution of the spatial amplitude, $S(x, y)$, and (b) distribution of the spatial phase, $\theta(x, y)$, for the first mode in the CEOF analysis. Large amplitudes are found at the footpoint and at the lower edge of the loop. It is also possible to identify some filamentary structures inside the loop. A phase difference of π is also evident between the upper and lower edges of the loop. [See the electronic edition of the *Journal* for a color version of this figure.]

increasing from the footpoint of the loop and delineating its shape. This is in perfect correspondence with the results shown in Figure 3 for the mode, which explains the propagating part of the synthetic signal. Note that in principle, from the CEOF analysis the phase gradient allows to calculate the two-dimensional wavevector field corresponding to the propagating feature. Nevertheless, as we can see in Figures 8c and 8d, although the spatial phase shows a global increase, it also displays small-scale variations, so the computation of the gradient results in a rather random wavevector field. For this reason, we have calculated the wavelength by estimating the derivative of the phase with position along two particular paths. The selected paths, one for each of the two CEOF modes, originate at the footpoint of the loop and extend along it (see the dashed lines in Figs. 8c and 8d). In Figure 9 we can see the spatial phases for the different paths, together with a linear fit that has been used to estimate the wavelengths, which are 24,000 and 33,000 km (this procedure gives only a lower limit of the wavelength because of projection effects along the line of sight). It is possible to carry out an estimation of the phase velocity with the usual expression $v_{\text{ph}} = \lambda/P$, which by using a period of 5.3 and 4.3 minutes for the third and fourth modes gives phase velocities of 78 and 125 km s⁻¹, respectively. Such a difference in the phase speed for the two paths is mostly a consequence of the nonstationary behavior of the propagating feature. Note also that the “noisy” character of the phase can also produce differences in the estimation of the phase speed for the two paths.

4.2. Oscillations with Period ~ 10 minutes

The CEOF mode with a period of 10.6 minutes accounts for 26.8% of the total variance of the “filtered” signal. We have proceeded as in the previous section and have constructed a movie with the spatiotemporal variation of this mode, shown in the middle panel of Movie 2. The movie shows large intensity fluctuations at the footpoint of the loop, although the most interesting feature is that oscillations seem to be located in narrow (around 2'') and long structures. Figure 10 displays some frames of the movie for different times, and it is possible to identify some of these thin threads inside the loop. Note that they oscillate coherently with a period that is ~ 10 minutes and seem to be quite stationary in time. These thin structures have their origin at the footpoint and from this position extend to large distances along the loop. The typical separation between these structures is 2''.

The temporal information contained in this CEOF mode (see Fig. 6) indicates that the amplitude takes its maximum value at

about one-half the observational time, while at the beginning and end of the temporal series it has lower values, which arise from the end effects in the estimation of the Hilbert transform. The temporal phase, on the other hand, clearly indicates a strong periodicity and allows estimation of the period of oscillation of this mode, which is 10.6 minutes. The spatial amplitude distribution (see Fig. 11a) delineates a filamentary structure inside the loop that is especially clear in the center (around $x = 30$, $y = 30$). Note also that larger amplitudes are found only on the lower edge of the loop and in the region around the footpoint of the structure. Moreover, the spatial phase reveals (see Fig. 11b) that the phase difference between both edges of the loop is π , which may be a signature of a standing wave motion (see § 3). This issue is discussed in more detail in the next section.

5. DISCUSSION AND CONCLUSIONS

The main aim of this paper is to demonstrate the potential of the joint application of the EMD and CEOF techniques in the analysis of coronal oscillations. The EMD analysis technique effectively isolates the different timescales in temporal series, and its application as a filter allows us to determine with great detail, even for noisy signals, the spatial distribution of oscillatory motions with no sacrifice in spatial or temporal resolution. It has also been shown that with the help of the CEOF technique the global features of a data set that correspond to standing and propagating patterns can be isolated and that, more importantly, quantitative data about waves, such as the period, wavelength, two-dimensional spatial distribution of amplitudes, etc., can be obtained. In this respect, the two-dimensional study of oscillations in loops has not been addressed in previous works, but we have shown that it is possible to obtain interesting information in two dimensions and in consequence to gain further insight from observational data.

Regarding the analysis of the loop, we have found oscillations with a period of ~ 5 minutes. They originate at the footpoint and clearly propagate outward along the loop. This result is similar to that found by Berghmans & Clette (1999), Robbrecht et al. (2001), and De Moortel et al. (2000), in the latter case for the same loop. The CEOF analysis gives a decomposition of this feature in two modes that account for more than 20% of the variance of the field and provide, for the first time, two-dimensional information about the spatial distribution of the amplitude inside the loop. Large amplitudes occur close to the footpoint, and the CEOF method indicates the existence of a strong correlation between the periodicity found there and the propagating feature along the loop. This is also in

agreement with Berghmans & Clette (1999), who found that many of the traveling disturbances along open field lines originate from weak EUV brightenings at the footpoints.

The third and fourth modes decomposed with the CEOF technique have allowed us to compute the wavelength associated with the propagating feature. This magnitude has been estimated to have a value of 29,000 km (mean value of the two paths considered), while the phase velocity is approximately 100 km s^{-1} (this is a lower limit because of projection effects). As intensity variations can be associated with density fluctuations, the propagating disturbances seem to be of a compressional nature. Moreover, since the traveling features propagate at a speed of the order of the typical coronal sound speed, which is 166 km s^{-1} for a fully ionized plasma with 10^6 K temperature, the detected propagating perturbations can be interpreted as slow magnetoacoustic waves (see De Moortel et al. 2000).

We have also found intensity fluctuations with a period of 10.6 minutes and a rather different behavior. Oscillations with this period show a strong stationary character, such as has been confirmed by the application of the CEOF technique. The spatial distribution of the amplitude of this mode indicates that large values are located at the edges of the loop but also in thin and long structures in the loop center. Although the main motivation of this paper is not to interpret these features, it is worth making a comment on these stationary oscillations. The fact that the edges of the loop show large intensity variations can indicate that it oscillates as a whole transversally around the equilibrium position in the so-called fundamental kink mode of oscillation (see Edwin & Roberts 1983). For this oscillation mode, strong periodic intensity variations are pro-

duced precisely at the position of the unperturbed edge, while the intensity remains almost unchanged at the loop center. In addition, with the CEOF analysis we have found that there are π phase differences between the edges of the loop, which further supports the hypothesis of the standing kink mode being responsible for the 10.6 minute oscillations. Nevertheless, one should not forget that density fluctuations are also localized in thin and long structures originating at the footpoint and distributed over the loop width. A possible explanation is that these thin structures are the consequence of a radial harmonic of the kink mode of oscillation. For such a mode, additional density fluctuations to those located at the edges of the loop are present in concentric layers of the tube. However, further analysis is necessary to test this hypothesis, since the effects of projection and integration along the line of sight can have a strong influence on the possible detection of this mode. Another possible interpretation of this kind of localized fluctuations is that they are associated with the internal structure of the loop. Although the loop apparently shows a bright and compact shape, it may be formed by several thin tubes, in slightly different physical conditions, that delineate the magnetic field lines (see Reale & Peres 2000). Thus, these oscillations may reflect the multithread structure of the loop.

The authors thank M. J. Aschwanden and A. W. Hood for useful discussions and the Spanish Ministry of Science and Technology for the funding provided under grant AYA2003-00123.

REFERENCES

- Aschwanden, M. J., Nightingale, R. W., Tarbell, T. D., & Wolfson, C. J. 2000, *ApJ*, 535, 1027
- Banerjee, D., O'Shea, E., & Doyle, J. G. 2000, *A&A*, 355, 1152
- Berghmans, D., & Clette, F. 1999, *Sol. Phys.*, 186, 207
- DeForest, C. E., & Gurman, J. B. 1998, *ApJ*, 501, L217
- De Moortel, I., Hood, A. W., & Ireland, J. 2002a, *A&A*, 381, 311
- De Moortel, I., Ireland, J., Hood, A. W., & Walsh, R. W. 2002b, *A&A*, 387, L13
- De Moortel, I., Ireland, J., & Walsh, R. W. 2000, *A&A*, 355, L23
- De Moortel, I., Ireland, J., Walsh, R. W., & Hood, A. W. 2002c, *Sol. Phys.*, 209, 61
- Domingo, V., Fleck, B., & Poland, A. I. 1995, *Sol. Phys.*, 162, 1
- Edwin, P. M., & Roberts, B. 1983, *Sol. Phys.*, 88, 179
- Freeland, S. L., & Handy, B. N. 1998, *Sol. Phys.*, 182, 497
- Handy, B. N., et al. 1999, *Sol. Phys.*, 187, 229
- Horel, J. D. 1984, *J. Climate Appl. Meteor.*, 23, 1660
- Huang, N. E., Shen, Z., & Long, S. R. 1999, *Annu. Rev. Fluid Mech.*, 31, 417
- Huang, N. E., et al. 1998, *Proc. R. Soc. London A*, 454, 903
- Komm, R. W., Hill, F., & Howe, R. 2001, *ApJ*, 558, 428
- Ofman, L., Romoli, M., Poletto, G., Noci, C., & Kohl, J. L. 2000, *ApJ*, 529, 592
- O'Shea, E., Banerjee, D., Doyle, J. G., Fleck, B., & Murtagh, F. 2001, *A&A*, 368, 1095
- Reale, F., & Peres, G. 2000, *ApJ*, 528, L45
- Robbrecht, E., Verwichte, E., Berghmans, D., Hochedez, J. F., Poedts, S., & Nakariakov, V. M. 2001, *A&A*, 370, 591
- Terradas, J., Molowny-Horas, R., Wiehr, E., Balthasar, H., Oliver, R., & Ballester, J. L. 2002, *A&A*, 393, 637
- von Storch, H., & Zwiers, F. W. 1999, *Statistical Analysis in Climate Research* (Cambridge: Cambridge Univ. Press)
- Wallace, J. M., & Dickinson, R. E. 1972, *J. Appl. Meteor.*, 11, 887